



Ultra-high resolution regional climate projections for assessing changes in hydrological extremes and underlying uncertainties

Y. Qing¹ · S. Wang^{1,2} · B. Zhang¹ · Y. Wang³

Received: 10 March 2020 / Accepted: 9 July 2020
© Springer-Verlag GmbH Germany, part of Springer Nature 2020

Abstract

The frequency and intensity of extreme hydrological events (droughts and floods) have been increasing over the past few decades, which has been posing a threat to water security and agriculture production. Thus, projecting the future evolution of hydrological extremes plays a crucial role in sustainable water management and agriculture development in a changing climate. In this study, we develop the high-resolution projections of multidimensional drought characteristics and flood risks using the convection-permitting Weather Research and Forecasting (WRF) model with the horizontal grid spacing of 4 km for the Blanco and Mission River basins over South Texas. Uncertainties in model parameters are addressed explicitly, thereby leading to probabilistic assessments of hydrological extremes. Our findings reveal that the probabilistic multivariate assessments of drought and flood risks can reduce the underestimation and the biased conclusions generated from the univariate assessment. Furthermore, our findings disclose that future droughts are expected to become more severe over South Texas even though the frequency of the occurrence of droughts is projected to decrease, especially for the long-term drought episodes. In addition, South Texas region is expected to experience more floods with an increasing river discharge. Moreover, the Blanco and Mission river basins will suffer from higher flood risks as flood return periods are expected to become longer under climate change.

Keywords Regional climate projection · Hydrological extremes · Drought · Flood · Copula

1 Introduction

Extreme hydrological events (droughts and floods) have been one of the most dangerous and expensive natural disasters associated with climate change and human activities, which can cause significant losses, especially in water resources, agriculture, environment, and social economy (Raziel et al. 2009; Mishra and Singh 2010; Xiao et al. 2016;

Zuo et al. 2016; Li et al. 2019; Chen et al. 2020). During the past few decades, hydrological extremes have become more intense and frequent around the world in a changing climate, which has been receiving great attention from the hydroclimate community (Parry et al. 2007). Hence, assessing the dynamic evolution of hydrological extremes is necessary to mitigate extreme hazards, which plays a crucial role in water resources systems planning and agriculture development.

Numerous studies have been conducted to develop techniques for assessing droughts and floods over the past decades (De Michele et al. 2005; Chebana et al. 2009; Tabari et al. 2013; Waseem et al. 2016; Miah et al. 2017; Carvalho and Wang 2019). As for the drought assessment, drought indices are widely used as an effective means to detect and to analyze droughts. Generally, standardized precipitation index (SPI) and standardized precipitation evapotranspiration index (SPEI) are used to represent meteorological droughts (Lloyd-Hughes and Saunders 2002; Vicente-Serrano et al. 2011). Standardized runoff index (SRI) and streamflow drought index (SDI) are used to characterize hydrological drought hazards (Shukla and Wood 2008;

Electronic supplementary material The online version of this article (<https://doi.org/10.1007/s00382-020-05372-6>) contains supplementary material, which is available to authorized users.

✉ S. Wang
shuo.s.wang@polyu.edu.hk

¹ Department of Land Surveying and Geo-Informatics, The Hong Kong Polytechnic University, Hong Kong, China

² The Hong Kong Polytechnic University Shenzhen Research Institute, Shenzhen, China

³ Department of Geosciences, Texas Tech University, Lubbock, TX, USA

Nalbantis and Tsakiris 2009). And agricultural drought analysis relies on standardized soil moisture index (SSI) (Vicente-Serrano et al. 2011). To assess flood events, a variety of probability distributions, including normal (Goel et al. 1998), lognormal (Yue 2000), exponential (Favre et al. 2004), gamma (Yue 2001), and extreme value distributions (Adamson et al. 1999), are commonly used to model flood characteristics.

Drought is a multivariate phenomenon related to a series of complex and interactive hydroclimatic variables (e.g., precipitation, temperature, and runoff). When a single index is used to characterize drought events, potential interrelationships of drought variables can be neglected, thereby resulting in erroneous or biased conclusions about the occurrence and severity of drought events (Mishra and Singh 2010; Hao and AghaKouchak 2013; Hao and Singh 2015; Flint et al. 2018; Chen et al. 2019; Zhang et al. 2019). In addition, flood is often characterized by peak (P), volume (V) and duration (D). And these flood variables are actually correlated with each other. Thus, multivariate analysis techniques have been attracting increasing attention for improving the robustness and reliability of drought and flood risk assessments.

Copulas are being widely used in multivariate analysis of hydrological extremes, which is recognized as a powerful means to characterize droughts and floods through constructing a multivariate distribution based on multiple univariate distributions (De Michele and Sal-vadori 2003; Favre et al. 2004; Genest and Favre 2007; Kao and Govindaraju 2010; Hao and AghaKouchak 2013; Salvadori and De Michele 2015; Cheraghalizadeh et al. 2018). Nevertheless, little effort has been made to improve the estimation of copula parameters. Since local optimization methods often get trapped in local minima for estimating copula parameters, the derived copulas are often biased (Kwon and Lall 2016). In addition, the other factors, such as short data records, can bring parameter uncertainty in copulas (Sadegh et al. 2017). It is thus necessary to increase the reliability of multivariate assessments of droughts and floods by improving copula construction.

In addition to examining drought and flood episodes in the past, it is vital to project future changes of drought and flood characteristics in a changing climate. Projecting drought and flood evolutions plays a key role in hazard mitigation and adaptation (Song et al. 2015; Zhang et al. 2015; Hao et al. 2017). Future hydroclimatic information is often obtained using general circulation models (GCMs) or regional climate models (RCMs) (Sexton et al. 2001; Karri et al. 2018; Zhu et al. 2019; Wang and Zhu 2020). Nevertheless, both GCMs and RCMs can hardly represent the local-scale physical processes and spatial heterogeneity due to the relatively coarse spatial resolution. In addition, it is suggested that climate models with the use of convection parameterization schemes can cause large errors and

uncertainties in climate simulations associated with convection processes (Lange et al. 2015; Prein et al. 2015). As a result, the convection-permitting climate modeling with high spatial resolution has been receiving great attention to explicitly resolve convection processes, which is a promising climate modeling technique for producing high-resolution and reliable climate information, especially for precipitation which is the most important factor affecting droughts and floods (Wagner et al. 2013; Kay et al. 2015). On the other hand, numerous studies have proved that the probabilistic hydrological prediction is superior to the deterministic prediction due to various sources of uncertainty in hydrological modeling (DeChant and Moradkhani 2015; Wang et al. 2018; Wang and Wang 2019).

The aim of this study is to develop probabilistic projections of future changes in multivariate drought and flood characteristics through the convection-permitting Weather Research and Forecasting (WRF) modeling system. A scenario-based hydrometeorological drought index (SHDI) will be developed to examine the joint effect of meteorological and hydrological droughts. In addition, the joint effect of flood peak and volume will be examined to assess flood risks. Model parameter uncertainties will also be addressed explicitly, leading to probabilistic projections of multivariate drought and flood characteristics. The probabilistic drought and flood projections will be conducted for the two major river basins in Texas of the United States. The Parameter-elevation Regressions on Independent Slopes Model (PRISM) dataset will be used to verify the high-resolution WRF simulations. The Model Parameter Estimation Experiment (MOPEX) dataset will be utilized to perform hydrological simulations. The United States Geological Survey (USGS) gauging station data will also be used to calibrate and validate the hydrological model.

This paper is organized as follows. In Sect. 2, algorithms, model configurations, and datasets will be described. In Sect. 3, assessments of the copula-based SHDI, multivariate flood risks, as well as the convection-permitting WRF simulation will be provided. In addition, a thorough discussion on uncertainty quantification of drought and flood assessments will be presented. In Sect. 4, conclusions and key findings will be drawn.

2 Algorithms, models and data sources

2.1 Univariate drought indices

In this study, two univariate drought indices including SPEI and SRI were jointly used to assess drought episodes across different temporal scales. SPEI is an index of meteorological drought, which represents the climatic water balance. It is defined as the difference between monthly precipitation

and potential evapotranspiration (PET), and can be derived according to the computational procedure of SPI. As PET is calculated based on multiple variables including relative humidity, wind speed, solar radiation, and air temperature (Allen et al. 1998), a number of approaches have been developed to estimate PET. Among these, the Penman–Monteith approach has been widely used and has been adopted by the Food and Agriculture Organization of the United Nations (FAO) as the standard procedure of computing PET. The FAO-56 Penman–Monteith equation was applied to estimate PET based on climate information obtained from the convection-permitting WRF simulation. Based on the simulated monthly precipitation and PET each year, their difference can be calculated using:

$$D_{ij} = P_{ij} - PET_{ij} \quad (1)$$

where P_{ij} is precipitation of the i th year and the j th month, and PET_{ij} is potential evapotranspiration of the i th year and the j th month.

According to Eq. (1), the SPEI value for each temporal scale can be calculated as follows:

$$D_l = D_{ij} = (i - i_0) \times 12 + j, \quad (2)$$

$$X_l^k = \sum_{l=k+1}^l D_l, \quad (3)$$

$$X_{ij}^k = X_l^k i = i_0 + \text{int} \left[\frac{l-1}{12} \right] j = \text{mod}[(l-1), 12] + 1. \quad (4)$$

where X_{ij}^k represents the SPEI value derived at temporal scale k . l is the l th month ($l \in [1, 180]$), and i_0 is the initial year. SRI can be used to describe the hydrological drought based on the monthly runoff in a specific river basin. The SRI value can be calculated using the similar procedure of calculating SPI based on the streamflow time series (Shukla and Wood 2008).

2.2 Scenario-based hydrometeorological drought index with uncertainty intervals

Due to the existence of potential interactions between drought characteristics, we propose a scenario-based hydrometeorological drought index (SHDI) that takes into account the joint effect of hydroclimatic variables including precipitation, PET, and runoff. Such a hydrometeorological drought index is able to simultaneously characterize different types of droughts including meteorological (SPEI) and hydrological droughts (SRI) as well as their interactions. Given that SPEI and SRI can be represented by X and Y , there exists a copula, C , that combines the two marginal distributions to

generate the joint cumulative distribution function (CDF), P , as follows:

$$P(X \leq x, Y \leq y) = C[F(X), G(Y)] = p, \quad (5)$$

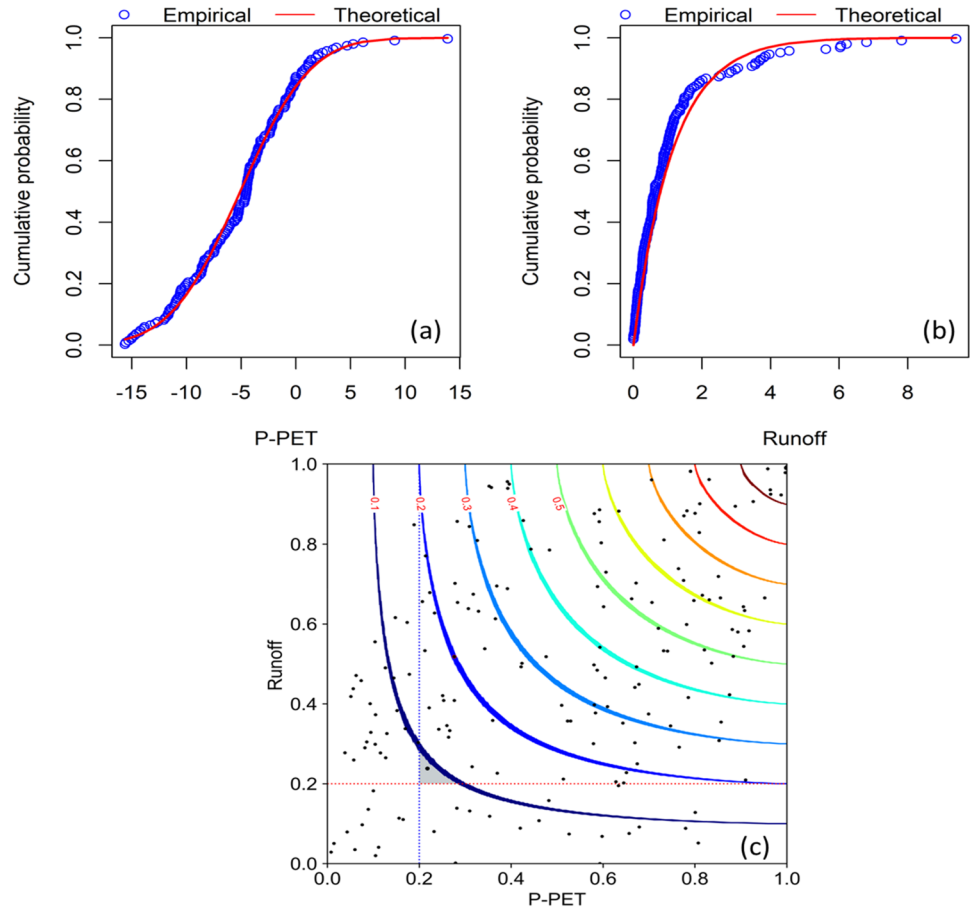
where $C[F(X), G(Y)]$ is the bivariate copula function. $F(X)$ and $G(Y)$ are the marginal CDFs of X and Y , respectively. The SHDI value is then calculated by taking the inverse normal of p :

$$\text{SHDI} = \varphi^{-1}(p). \quad (6)$$

Specifically, to construct multivariate drought indices, the marginal distributions of P–PET which is the difference between precipitation (P) and potential evapotranspiration (PET) as well as runoff are constructed (Fig. 1a, b). A total of 16 types of probability distributions, including Birnbaum–Saunders, Exponential, Extreme Value, Gamma, Generalized Extreme Value (GEV), Generalized Pareto, Inverse Gaussian, Logistic, Loglogistic, Lognormal, Nakagami, Normal, Rayleigh, Rician, t Location-Scale, and Weibull were used to fit P–PET and runoff data. The optimal parameters for these probability distributions were estimated based on the statistical measure of AIC, BIC, and the AIC with a correction for finite sample sizes (AICc). The Frank, the Gumbel, and Clayton copulas were selected for determining the joint probability distributions of P–PET and runoff since they were extensively used to analyze drought characteristics (Kao and Govindaraju 2008; Kavianpour et al. 2018; Chen et al. 2019). The MCMC algorithm was used to address uncertainty in copula parameters, thereby leading to a scenario-based hydrometeorological drought index (SHDI) with probability isolines. The range of uncertainty in the probability isolines reflects the underlying uncertainty in the dependence structure of P–PET and runoff (Fig. 1c), which uncovers the potential risk in the joint assessment of drought episodes. The AIC, BIC, AICc, and maximum likelihood were calculated to choose the optimal copula. The root mean square error (RMSE) and the Nash–Sutcliffe efficiency (NSE) were also used to evaluate the performance of different copula families.

The SHDI with uncertainty intervals can be used to provide reliable and robust assessments of drought characteristics in terms of severity, duration, and intensity. The upper and lower bounds of uncertainty intervals represent the best- and the worst-case scenarios of a drought event, respectively (see Fig. S1 of the supplementary information). For the best-case drought scenario (-0.8 was the threshold used to detect droughts), the area between the threshold of -0.8 and the upper bound of uncertainty intervals represent the severity of droughts. For the worst-case drought scenario, the area between the threshold of -0.8 and the lower bound of uncertainty intervals represents the drought severity. It shows that the drought

Fig. 1 a, b Comparison between the theoretical CDFs and the empirical CDFs of P-PET and runoff. c SHDI with probability isolines



duration of the worst-case scenario is much longer than the best-case scenario. Meanwhile, the drought onset of the worst-case scenario is much earlier than the best-case scenario. This amplification of drought severity and drought duration by the SHDI with uncertainty intervals plays an important role in drought risk assessments and development of adaptation strategies.

In addition, the proposed SHDI is able to reduce the underestimation of drought risks and biased conclusions on drought episodes due to the use of univariate drought indices. For example, a given threshold of -0.8 is used to identify a drought event (see Fig. S1 of the supplementary information). It can be seen that a drought event can be identified using SPEI with a value smaller than -0.8 but cannot be determined by SRI. By contrast, SHDI captures the drought event, and the drought onset is earlier than those identified by SPEI and SRI under the worst-case scenario, explicitly uncovering the potential risk of assessing droughts by univariate indices. Thus, it is essential to pay close attention to interrelationships of different types of drought events and potential uncertainties in the dependence structure so as to gain a robust and reliable assessment of drought hazards.

2.3 Probabilistic flood risk assessment

The Peaks over Threshold (POT) approach was used in this study to sample flood events. The selection of the threshold u in the POT model is a prerequisite for the accurate estimation of parameters β and ζ , and it is essential to the effectiveness of the POT model. If the threshold is selected too high, the sample data used for analysis is too small, thereby resulting in unreliable results; if the threshold is selected too low, a significant bias can be caused due to the relatively low variance even though there is more data for analysis. To choose the optimal threshold, the hill plot combined with the exponential regression model was conducted. $H_{k,n}$ is a hill estimate for its extreme index, and the exponential regression model based on the hill estimation is shown as Eq. (8).

$$H_{k,n} = \frac{1}{k} \sum_{j=1}^k j(\log X_{n-j+1,n} - \log X_{n-j,n}), 1 \leq k \leq n - 1 \quad (7)$$

$$j(\log X_{n-j+1,n} - \log X_{n-j,n}) = \left(\gamma + b_{n,k} \left(\frac{j}{k+1} \right)^{-p} \right) f_j, 1 \leq j \leq k \quad (8)$$

where X_1, X_2, \dots, X_n are independent and identically distributed positive random variables, and their order statistics are $X_{1,n} \geq X_{2,n} \geq \dots \geq X_{n,n}$. Constant $\gamma > 0$, $\rho \leq 0$, $b_{n,k} = b(\frac{n+1}{k+1})$, $1 \leq k \leq n - 1$, and $b_{n,k}$ is a positive ratio function. f_1, f_2, \dots, f_k is a series of random variables that are independent of each other and follow a standard exponential distribution. A reasonable value of k is chosen according to the asymptotic mean square error (AMSE) minimum principle of hill estimation. The AMSE of hill estimation and the optimal k value can be calculated by Eqs. (9) and (10):

$$AMSE(H_{k,n}) = \left(\frac{b_{n,k}}{1 - \rho} \right)^2 + \frac{\gamma^2}{k} \tag{9}$$

$$k_n = \arg \min_k AMSE(H_{k,n}) = \arg \min_k \left(\left(\frac{b_{n,k}}{1 - \rho} \right)^2 + \frac{\gamma^2}{k} \right) \tag{10}$$

$u = X_{n-k,n}$ is the selected threshold. When the threshold of flood peak is selected, the corresponding hydrograph is used to determine the associated flood volume. The abrupt change points before and after the peak in each hydrograph are identified as the start and end of each flood event, respectively.

Based on the chosen flood peak and volume, the associated return period of each flood event can be derived through the constructed copula described in Sect. 2.2. Two widely used cases of flood return period are “AND” and “OR” cases. The OR return period (T_{OR}) refers to that at least one of flood peak (P) and volume (V) exceeds their respective thresholds, while the AND return period (T_{AND}) refers to that the two flood variables exceed their respective thresholds simultaneously. T_{OR} and T_{AND} can be defined as Eqs. (11) and (12), respectively:

$$T_{OR} = \frac{1}{P(X > x \vee Y > y)} = \frac{1}{1 - C(F_X(x), F_Y(y))} \tag{11}$$

$$T_{AND} = \frac{1}{P(X \geq x \wedge Y \geq y)} = \frac{1}{1 - F_X(x) - F_Y(y) + C(F_X(x), F_Y(y))} \tag{12}$$

where $C(F_X(x), F_Y(y))$ is the bivariate copula function. $F_X(x)$ and $F_Y(y)$ are the marginal CDFs of X and Y, respectively. Due to the posterior distribution of copula parameters derived from the MCMC simulation, the return period is probabilistic with uncertainty intervals.

2.4 High-resolution hydroclimatic modeling

The WRF model v3.7.1 was applied to simulate regional climate change over Texas. As shown in Fig. 2, the model domain covers a region of 1520 km × 1400 km (380 × 350 grid points) and 51 vertical levels topped at 50 hPa, which has a horizontal resolution of 4 km. Such a high-resolution

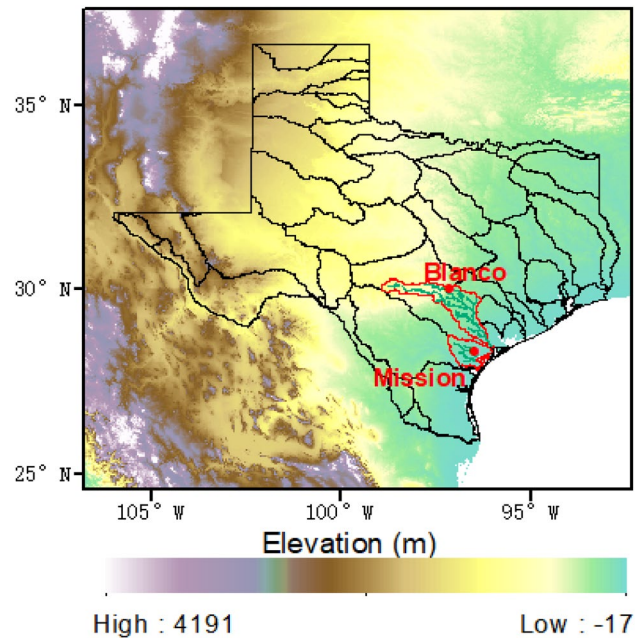


Fig. 2 Model domain with topography and the Blanco and the Mission River basins over South Texas. The red points represent the location of USGS gauging stations with long-term precipitation, PET, and streamflow records

model enables the explicit simulation of convection without the use of convection parameterization (Liu et al. 2011). The National Centers for Environmental Prediction (NCEP) Climate Forecast System Reanalysis (CFSR) that had a 0.5° × 0.5° spatial resolution was collected as the initial and lateral boundary conditions. The temporal resolution of model inputs and outputs were 6-h intervals. And model simulations were conducted over the 15-year period from January 1, 1981 through September 31, 1995. As for the experimental design, the model was configured with the Yonsei University planetary boundary layer scheme (Hong and Pan 1996), the Rapid Radiative Transfer Model (RRTMG) short-wave and long-wave radiation scheme (Iacono et al. 2008), the Thompson cloud microphysics scheme (Thompson et al. 2008), the Noah-MP land surface scheme (Niu et al. 2011; Yang et al. 2011), and the revised Monin–Obukhov surface layer scheme (Jiménez et al. 2012).

The high-resolution (4 km) future climate simulation was conducted over the period of 2085–2099, and the Pseudo-Global Warming (PGW) technique was applied to perturb the initial and boundary conditions of temperature, humidity, wind, soil temperature, geopotential fields, and sea level pressure (Liu et al. 2017). The climate perturbation was estimated by a multi-model ensemble mean climate change signal, which contained historical simulations for 1976–2005 and future projections for 2071–2100 under the Representative Concentration Pathway (RCP) 8.5 emission scenario, as shown in Eq. (13):

$$WRF_{input} = CFSR + (CMIP5_{2071-2100} - CMIP5_{1976-2005}). \tag{13}$$

A total of 15 CMIP5 GCMs were selected to produce the ensemble mean climate change signal in simulating the climate over North America (see Table S1 of the supplementary information). Based on the high-resolution projections of precipitation and PET through the WRF model, the hydrological simulations using the Hymod were carried out to predict daily streamflow in the Blanco and the Mission River basins over Texas (Fig. 2). The Hymod has been widely used to predict streamflow in various river basins with different hydroclimatic regimes around the world (Razavi and Gupta 2016; Abera et al. 2017; Roy et al. 2017). It operates based on a probability-distributed soil moisture storage capacity principle (Moore 1985). The distribution function of storage capacity is defined as:

$$F(C) = 1 - \left(1 - \frac{C}{C_{max}}\right)^{b_{exp}} \quad 0 \leq C \leq C_{max}. \tag{14}$$

All model parameters were initially given with an uncertainty range as shown in Table S2 of the supplementary information, and were calibrated against observations. The Markov chain Monte Carlo (MCMC) algorithm was used to address uncertainty in both hydrological model parameters and copula parameters. Such two layers of uncertainty lead to probabilistic projections of multivariate drought and flood characteristics. The MCMC algorithm is an effective tool used to estimate parameter densities by means of a Bayesian method, and the posterior distributions of model parameters can be inferred by recursively updating information in the prior parameter distributions when new observations become available:

$$P(\theta|\tilde{Y}) = \frac{P(\theta)P(\tilde{Y}|\theta)}{P(\tilde{Y})}, \tag{15}$$

$$P(\theta|\tilde{Y}) \propto P(\theta)L(\theta|\tilde{Y}), \tag{16}$$

where $P(\theta)$ and $P(\theta|\tilde{Y})$ represent prior and posterior distributions of model parameters, respectively, and $P(\tilde{Y}|\theta) \cong L(\theta|\tilde{Y})$ is the likelihood function. As $P(\tilde{Y})$ can be treated as a normalization constant, Eq. (15) can be simplified as Eq. (16). In Eq. (16), $L(\theta|\tilde{Y})$ denotes the likelihood function that quantifies the probability of the observation data and simulations. If the error residuals are uncorrelated, Gaussian-distributed, and homoscedastic, the likelihood function can be formulated as follow:

$$L(\theta|\tilde{Y}) = \prod_{t=1}^n \frac{1}{\sqrt{2\pi\tilde{\sigma}^2}} \exp\left\{-\frac{1}{2}\tilde{\sigma}^{-2}[\tilde{y}_t - y_t(\theta)]^2\right\}, \tag{17}$$

where $\tilde{\sigma}$ denotes the estimated standard deviation of measurement error, \tilde{y}_t is the observation at time t , and $y_t(\theta)$

is the model simulation given parameter θ at time t . For algebraic simplicity and numerical stability, Eq. (17) can be transformed to:

$$L(\theta|\tilde{Y}) = -\frac{n}{2} \ln(2\pi) - \frac{n}{2} \ln \tilde{\sigma}^2 - \frac{1}{2}\tilde{\sigma}^{-2} \sum_{t=1}^n [\tilde{y}_t - y_t(\theta)]^2. \tag{18}$$

When the prior distributions of model parameters and the likelihood function are determined, the posterior parameter distributions can be derived using the MCMC algorithm.

2.5 Data sources

The PRISM (Precipitation-elevation Regressions on Independent Slops Model), developed by the Oregon State University’s PRISM Climate Group using the “terrain-aware” interpolation techniques, was used to verify the accuracy of historical WRF simulations over Texas. It estimates precipitation on a spatial grid of 4 × 4 km resolution. The PRISM precipitation data from January 1981 to December 1995 were re-gridded to the 4-km domain for the purpose of comparison between simulated and observed data.

The MOPEX dataset was chosen to perform hydrological predictions for the Blanco and the Mission River basins located in South Texas over the period of January 1981 to December 1995. The 15-year dataset was divided into two parts. The first 10-year observations (from January 1981 to December 1990) were used to calibrate the hydrological model, and the remaining 5-year data (from January 1991 to December 1995) were used to validate hydrologic predictions. After model calibration and validation against observations, the hydrological model can be used to predict future streamflow regimes based on the projected precipitation and PET from the WRF model. Projecting streamflow plays an important role in assessing the complex evolution of droughts in a changing climate.

3 Results and discussion

3.1 Performance of copula-based SHDI in detecting droughts

In this study, we calculated P–PET and runoff across different timescales, and then fitted their corresponding probability density functions (PDFs). Different distributions were selected to fit the theoretical CDFs of P–PET and runoff, and then the statistical measures including AIC, BIC, AICc, and maximum likelihood were used to identify the optimal CDF (see Table S3 of the supplementary information). There is good agreement between the empirical CDFs and the theoretical CDFs, suggesting that the chosen distribution

Table 1 Assessment of copula functions

River	Temporal scale	Copula function	RMSE	NSE	Best copula
Blanco	3	Clayton	0.4538	0.9825	Gumbel
		Frank	0.4096	0.9858	
		Gumbel	0.3776	0.9879	
	9	Clayton	0.3146	0.9923	Gumbel
		Frank	0.1936	0.9971	
		Gumbel	0.1811	0.9975	
	15	Clayton	0.2867	0.9942	Frank
		Frank	0.1958	0.9973	
		Gumbel	0.2457	0.9958	
Mission	3	Clayton	0.6373	0.9659	Frank
		Frank	0.6275	0.9670	
		Gumbel	0.6578	0.9637	
	9	Clayton	0.2987	0.9930	Gumbel
		Frank	0.2756	0.9940	
		Gumbel	0.2639	0.9945	
	15	Clayton	0.3868	0.9876	Gumbel
		Frank	0.3437	0.9902	
		Gumbel	0.3201	0.9915	

functions are able to fit P–PET and runoff across all time-scales (see Figs. S2 and S3 of the supplementary information). To identify the optimal copula function, the three types of copula functions including Gumbel, Frank, and Clayton were compared against each other, and then the optimal copula function was selected based on NSE and RMSE. Table 1 presents the assessment of different copula functions used to characterize the dependence between P–PET and runoff at different temporal scales. To improve the reliability of the dependence structure of copula, the MCMC algorithm was used to address uncertainties in model parameters. Figure 3 depicts the marginal posterior distributions of copula parameters estimated for two river basins.

The copula-based SHDI was proposed to provide probabilistic assessments of multivariate droughts. It combined SPEI (meteorological drought index) and SRI (hydrological drought index) into a joint drought index using copula functions, which facilitates a thorough assessment of drought characteristics. Figure 4 compares the drought characteristics identified by univariate (i.e. SPEI and SRI) and multivariate (i.e. SHDI) drought indices at the timescales of 3, 9, 15 months for the Blanco and the Mission river basins. The changes of the SHDI values are similar to those of the SPEI

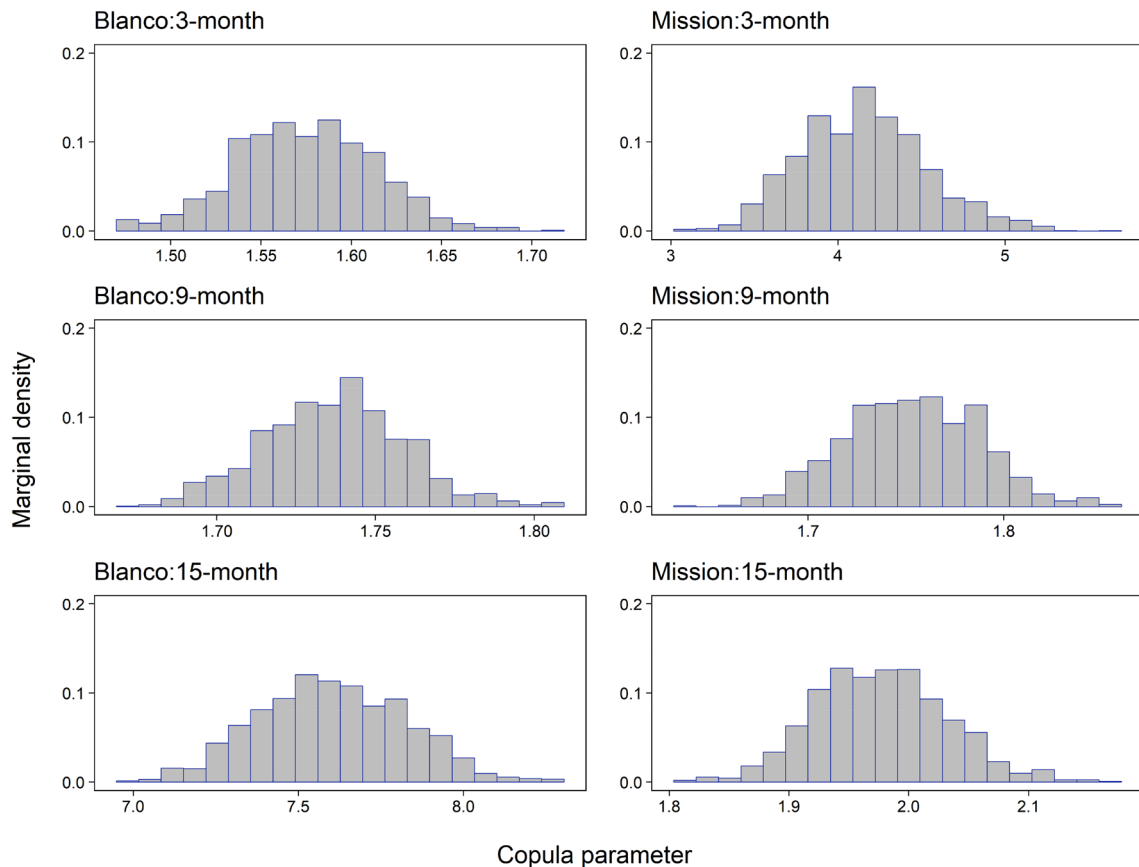


Fig. 3 Posterior distributions of copula parameters across different temporal scales

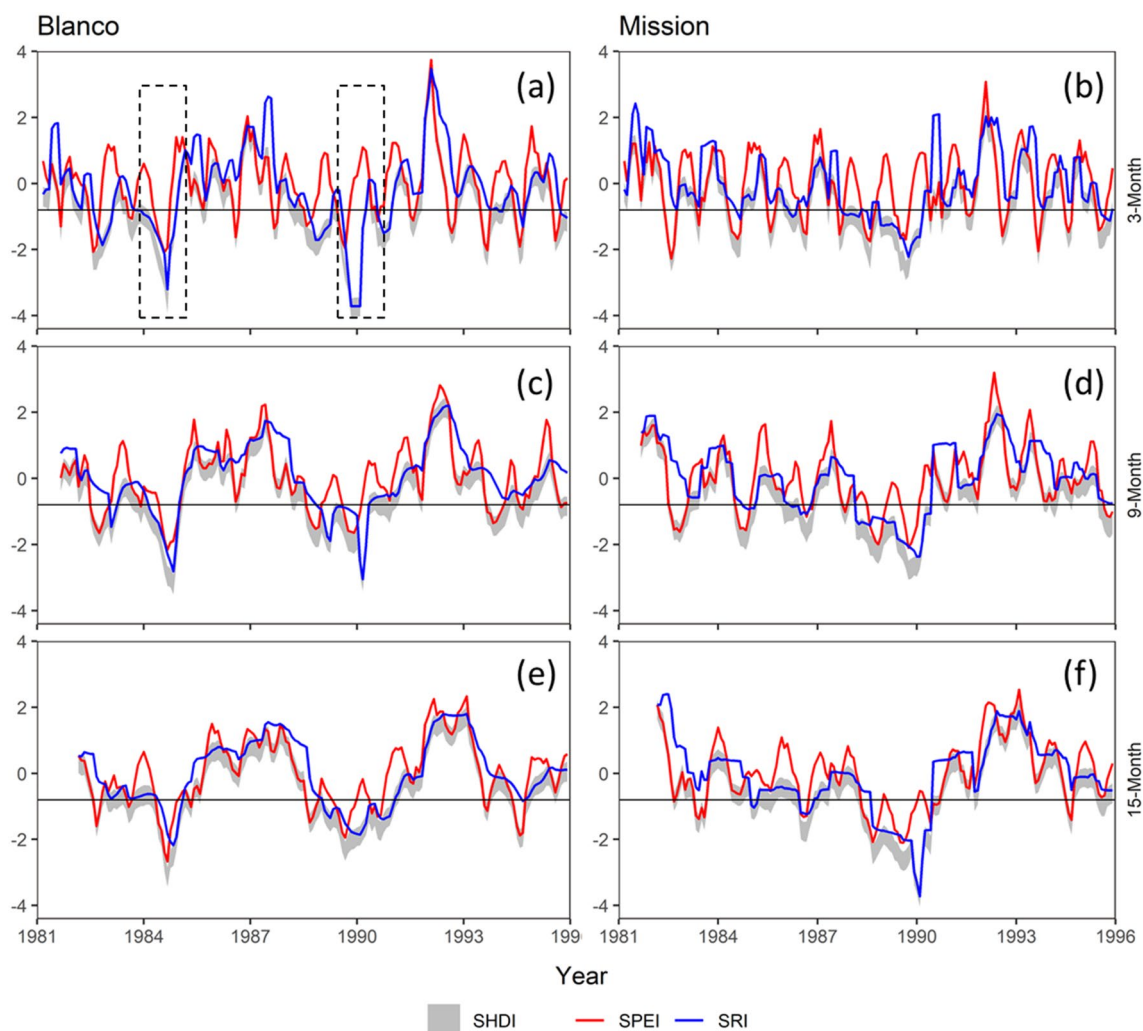


Fig. 4 Comparison of 3-, 9-, and 15-months SPEI, SRI, and SHDI. The y-axis represents the dimensionless values of SPEI, SRI, and SHDI

and the SRI values, suggesting that there is good agreement in the temporal trend of drought variations using SPEI, SRI, and SHDI.

The performance of SHDI in detecting multivariate drought characteristics was examined based on the following three aspects: (1) drought frequency, (2) drought duration, and (3) drought severity. To detect drought frequency and duration, the total number of drought events and the longest-duration drought events detected by SPEI and SRI are totally different. For example, for the Blanco river basin, the number of 3-, 9-, and 15-monthly drought events detected by SPEI is 14, 8, and 9, respectively. By contrast, the number of corresponding droughts identified by SRI is 8, 3, and 3, respectively. As shown in Fig. 4, our results reveal that droughts are underestimated and biased as a result of neglecting the joint effect of SPEI and SRI. It is thus necessary to develop a multivariate drought index in order to reduce potential underestimation and bias arising

from the use of univariate drought indices. As for the detection of drought severity, the SHDI values are derived with uncertainty intervals, leading to the best- and the worst-case scenarios of drought events. It should pay more attention to the worst-case scenario in practice because it offers a conservative assessment of drought severity, which can provide meaningful insights into drought mitigation and preparedness. For example, the average severity of 3-, 9-, and 15-months droughts under the worst-case scenario in the Mission river basin is -1.565 , -1.626 , and -1.805 , respectively. By contrast, the average severity of 3-, 9-, and 15-months drought events under the best-case scenarios is -1.289 , -1.408 , and -1.713 , respectively. As shown in Fig. 4, the SHDI values under the worst-case scenario are smaller than those of SPEI and SRI, indicating that the drought is expected to be more severe when considering the combined impact of hydrological and meteorological droughts. Such an amplification of the drought severity is

essential for mitigating the drought hazard and reducing the associated risk. The statistics of drought characteristics detected by SPEI, SRI, and SHDI are provided in Table S4 of the supplementary material.

On the other hand, the copula-based SHDI shows better skills in capturing extreme drought events in comparison with SPEI and SRI. For example, the two black dashed rectangles, as shown in Fig. 4a, depict two extreme short-term droughts that occurred in 1984 and 1990 in the Blanco river basin based on SHDI; however, such extreme droughts cannot be captured although two drought events are detected using SPEI. In addition, the proposed SHDI shows better skills in detecting extreme droughts across different time-scales. Since extreme droughts have widespread impacts on water security and environmental sustainability, the accurate monitoring of extreme droughts is necessary to reduce potential drought risks and associated losses.

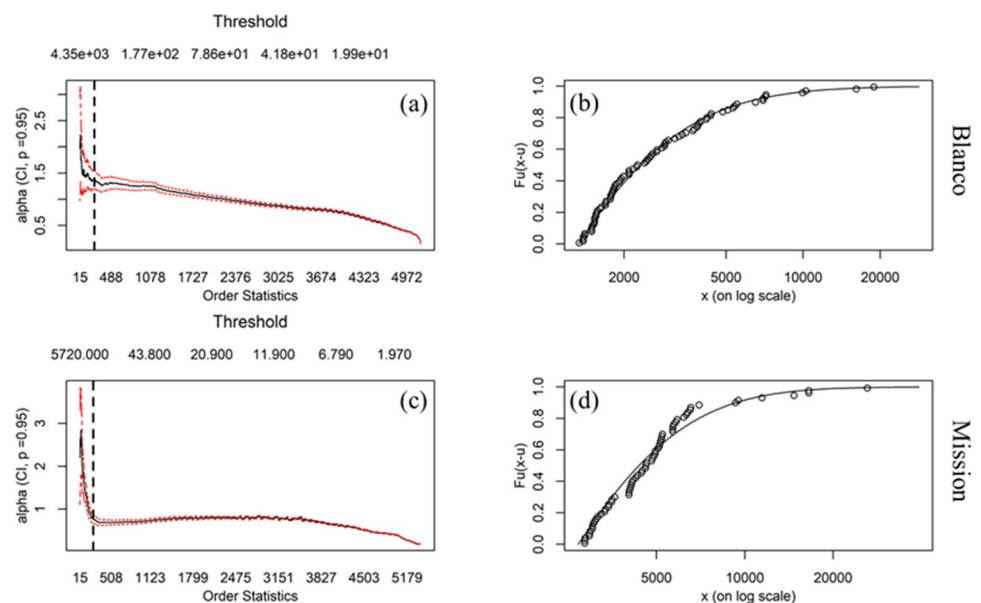
3.2 Performance of copulas in assessing flood risks

Flood events were identified using the approach introduced in Sect. 2.3. As shown in Fig. 5, a threshold is identified as the optimal flood peak threshold (black dashed lines represent the optimal thresholds). Thus, 1323.46 and 2705.25 ft³/s are the optimal flood peak thresholds for the Blanco and Mission river basins, respectively. This leads to 25 and 24 flood events, respectively, during 1981–1995. The corresponding flood volume is identified through the generated hydrographs. To robustly assess flood risk, the joint distributions were established based on flood peak and volume, and then the corresponding probability density functions (PDFs) were fitted. Same as drought assessments, a total of 13 different probability distributions were selected to fit

the theoretical CDFs of flood peak and volume, and then the optimal CDF was identified by AIC, BIC, AICc, and maximum likelihood (see Table S5 of the supplementary information). Fig. S4 of the supplementary material presents the comparison between the empirical CDFs and the theoretical CDFs of flood peak and volume over the Blanco and Mission river basins. Moreover, Gumbel, Frank, and Clayton copula functions were compared against each other, and then the optimal copula function was selected based on NSE and RMSE. Assessment of different copulas used to characterize the dependence between flood peak and volume can be seen in Table S6 of the supplementary material.

Uncertainties in model parameters are addressed through the probabilistic assessment of flood risks. Thus, uncertainty intervals exist in the estimation of flood return periods. Figure 6 presents the T_{OR} and T_{AND} return periods in the past (1981–1995) for the Blanco and Mission river basins. The Blanco and Mission river basins experienced 25 and 24 flood events, respectively. The mean T_{OR} and T_{AND} flood return periods for the Blanco river basin are larger than those for the Mission river basin. The mean T_{OR} and T_{AND} return periods for the Blanco river basin are 1.8 and 10.6 years, respectively; the corresponding return periods for the Mission river basin are 1.7 and 6.6 years, respectively. It should be noted that there is considerable uncertainty in the estimation of the T_{AND} return period for the Blanco river basin. And the largest uncertainty appeared in March 1992, lying within the range of 15–75 years. By contrast, the uncertainty intervals of the T_{AND} return period for the Mission river basin are relatively small, with the largest uncertainty range of 5–10 years that appeared in June 1981. In addition, the T_{OR} return period calculated by copulas is smaller than the return period derived based on the univariate flood risk assessment. For the flood event occurred

Fig. 5 The hill plots of daily streamflow (a, c) and the fitting diagnostic plots (b, d). The black dashed lines represent the chosen optimal threshold



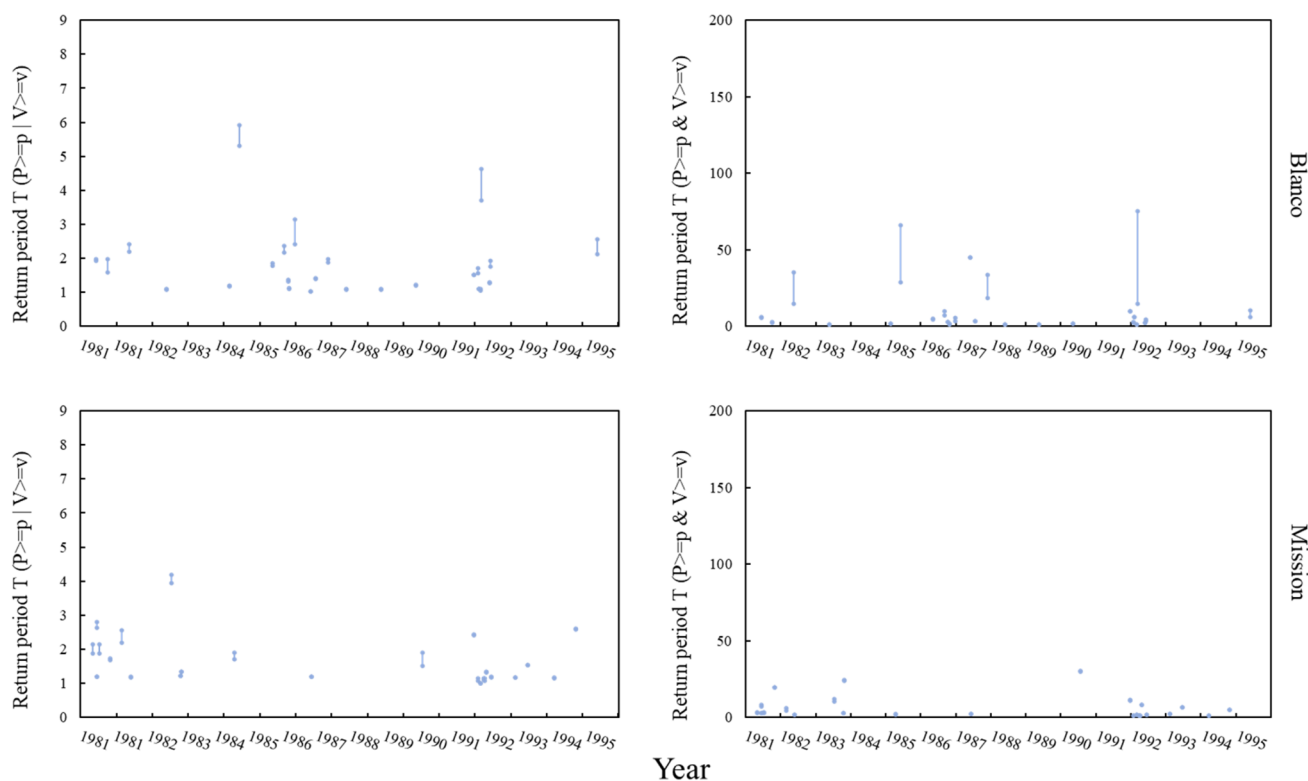


Fig. 6 Comparison of T_{OR} and T_{AND} flood return periods in the past for the Blanco and Mission river basins. The blue line represents the 95% uncertainty range of return periods

in September 1986 for the Blanco river basin, for example, the return periods of flood peak and flood volume are 5.5 and 2.6 years, respectively, depending on the univariate flood assessment. In fact, the T_{OR} return period of flood event lies within the range of 2.2–2.4 years, which is smaller than the univariate return periods. Considering the T_{AND} return period, the maximum return period is greater than the univariate return period, with the T_{AND} return period of 7.2–10.0 years. The similar findings are found for other pairs of hydrological variables. This indicates that we should pay more attention to the uncertainty intervals of T_{OR} and T_{AND} return periods than the univariate return period especially for the maximum value of uncertainty intervals, which provides meaningful insights into potential risks of hydrological extremes and high standards for flood design. Such a high flood magnitude estimated through multivariate flood risk assessment improves the reliability and safety of water conservancy projects, which plays a crucial role in reducing the damages caused by floods.

3.3 Validation and projection of high-resolution hydroclimatic simulations

To predict the changes of future drought and flood characteristics in a changing climate, the convection-permitting WRF simulations were performed to produce past and future

climate information including temperature, precipitation, and PET. The simulated climatic variables were compared with CFSR and PRISM datasets to demonstrate the performance of the convection-permitting climate modeling system. In general, the WRF model can well capture the spatial pattern of the past climate, especially for precipitation, due to the good performance on resolving the small-scale convective processes and capturing the spatial heterogeneity of precipitation.

Figures 7, 8, 9, and 10 present the spatial patterns of historical seasonal mean precipitation simulated by the WRF model, the CFSR production, the PRISM observation, as well as their absolute and relative differences for different seasons including spring (March–May, MAM), summer (June–August, JJA), fall (September–November, SON), and winter (December–February, DJF). In general, the WRF-simulated precipitation and the PRISM observation show good agreement, with the similar spatial distribution of seasonal mean precipitation. Specifically, the WRF model overestimates the spring precipitation over the study area (Fig. 7), but underestimates the summer, fall, and winter precipitation (Figs. 8, 9, 10). In comparison, the coarse-resolution CFSR generates much larger bias than the convection-permitting WRF model for simulating summertime precipitation (Fig. 8). The absolute difference between the

Fig. 7 Comparison of mean spring (MAM) precipitation from PRISM, CFSR, and WRF simulations

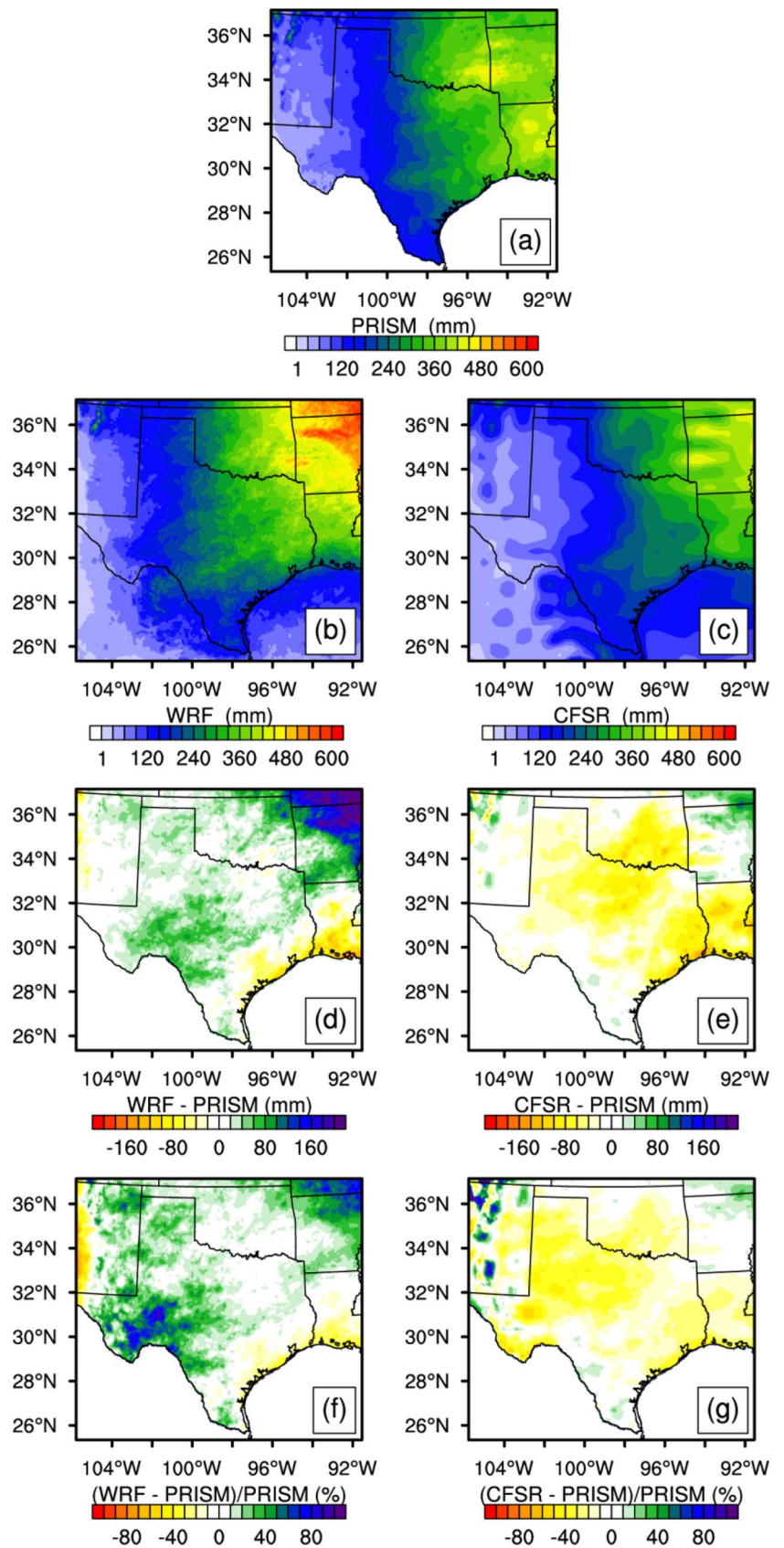


Fig. 8 Comparison of mean summer (JJA) precipitation from PRISM, CFSR, and WRF simulations

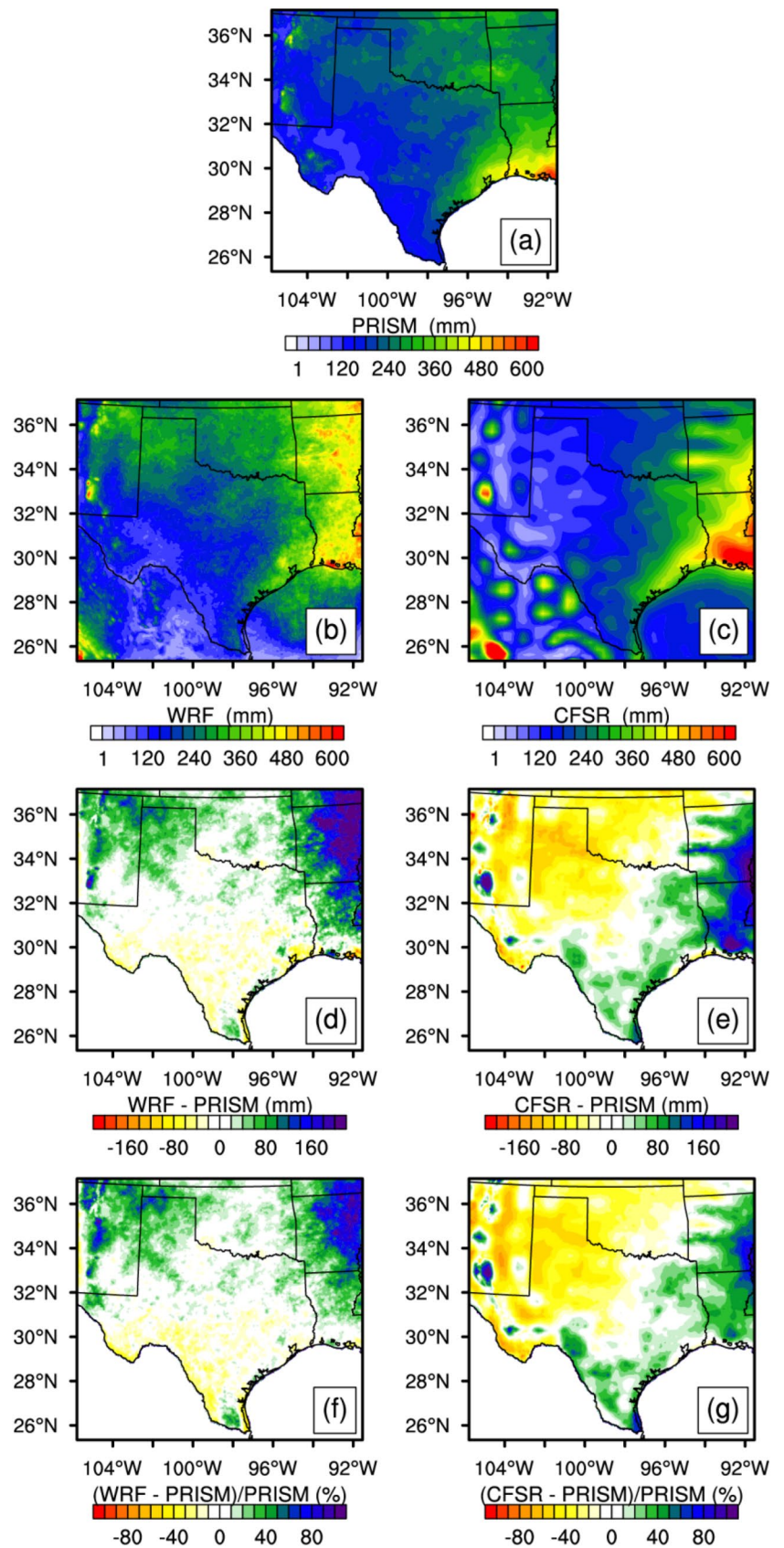


Fig. 9 Comparison of mean fall (SON) precipitation from PRISM, CFSR, and WRF simulations

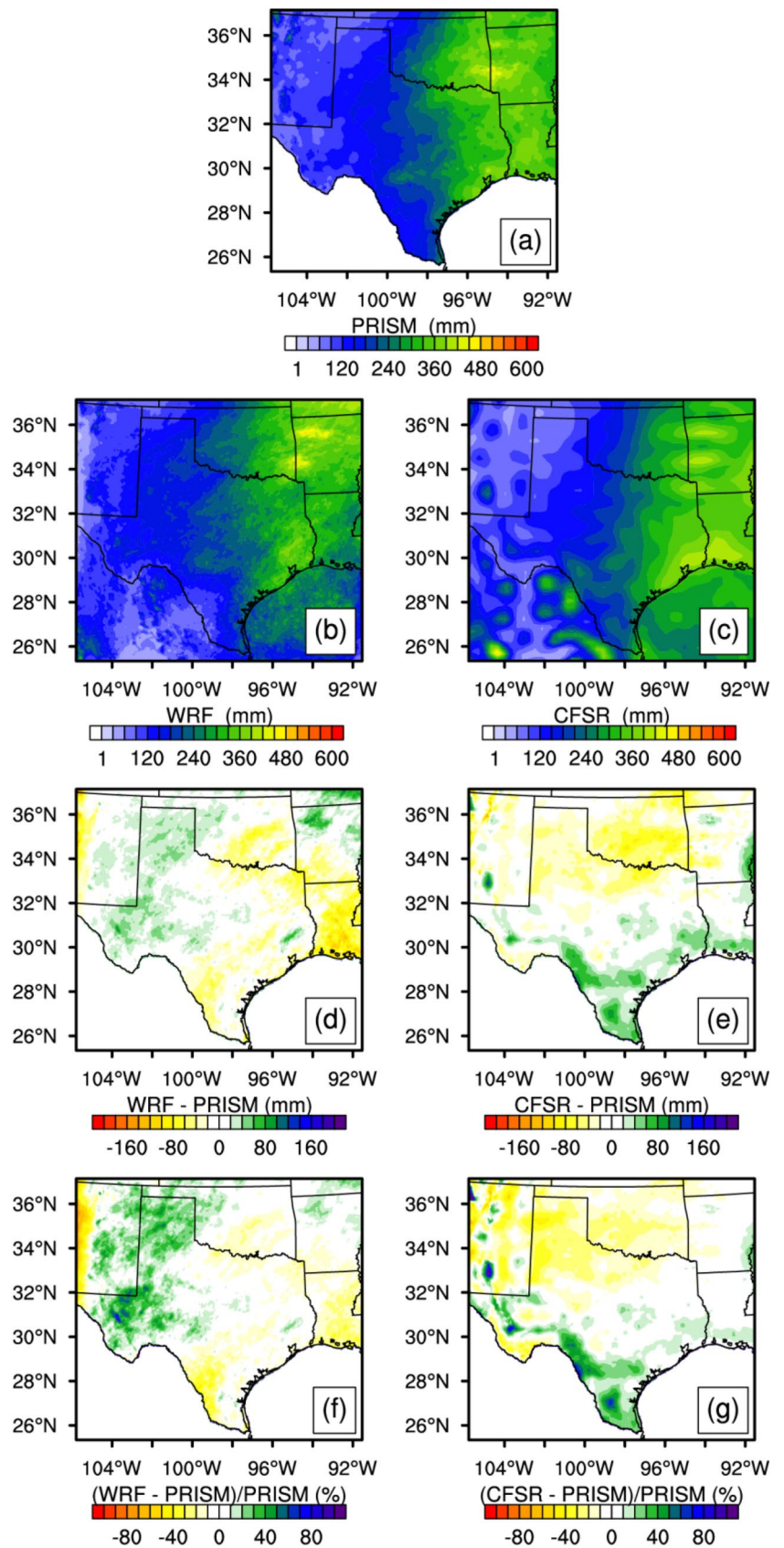
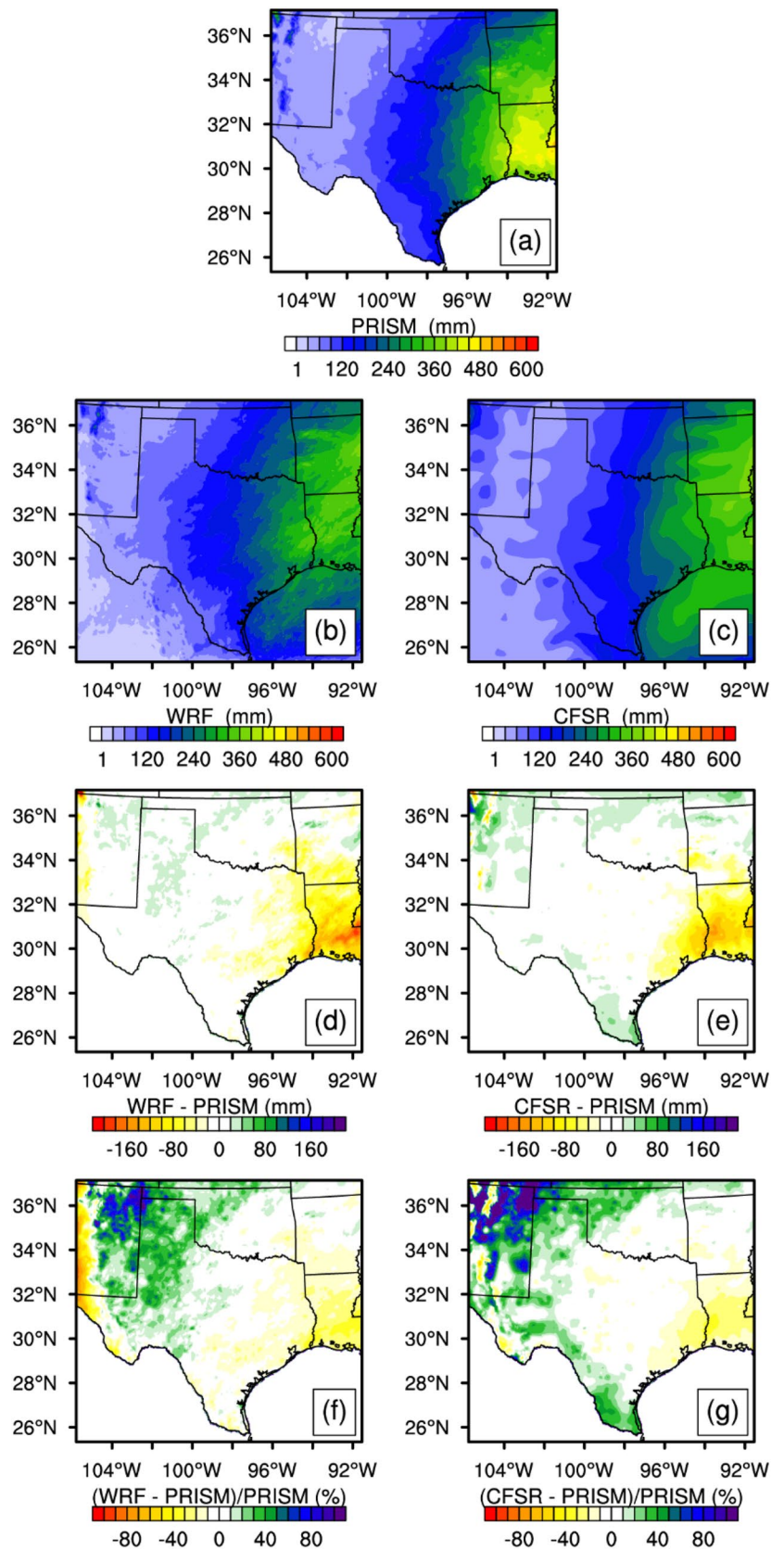


Fig. 10 Comparison of mean winter (DJF) precipitation from PRISM, CFSR, and WRF simulations



WRF model and the PRISM precipitation (WRF-PRISM) is smaller than the absolute difference between the CFSR and PRISM precipitation (CFSR-PRISM) for all seasons, especially for the summer season. Convective precipitation often occurs in summer, and thus it can be better simulated by the high-resolution convection-permitting WRF model. The accurate simulation of precipitation is crucial to enhancing the reliability of drought and flood assessments since precipitation is the most dominant variable causing droughts and floods.

The projected climate information was used to generate streamflow time series for the Blanco and the Mission river basins. The hydrological model was calibrated against streamflow observations from 1981 to 1990 and validated over a 5-year period of 1991–1995. The marginal posterior distributions of model parameters are provided in Fig. S5 of the supplementary material. The means and standard deviations of posterior parameter distributions are provided in Table S7 of the supplementary material.

Figure 11 depicts the predicted streamflow time series with the 95% uncertainty range in the calibration period of 1981–1990 and the validation period of 1991–1995 for the Blanco and the Mission river basins. In general, there is good agreement between streamflow observations and predictions during calibration and validation periods. For the calibration period, 85.1% and 90.1% of streamflow observations lie within the 95% uncertainty range of the predicted streamflow for the Blanco and the Mission river basins,

respectively. For the validation period, 84.1% and 85.9% of observations are captured for the Blanco and the Mission river basins, respectively. Such a large number of observations captured within the prediction intervals indicates that the hydrological model can be used to predict the future streamflow regimes based on the projected precipitation and PET. The projections of daily streamflow time series with a 95% uncertainty range for the future period of 2085–2099 are provided in Fig. S6 of the supplementary material.

Figure 12 shows the seasonal precipitation, PET, and streamflow variations over the period of 2085–2099. For the Blanco river basin, it can be seen that there will be a slight increase in the projected spring precipitation (Fig. 12a). In comparison, the winter, the summer, and fall precipitation are expected to decrease for 2085–2099. Specifically, the fall precipitation is projected to decrease significantly from 228.8 to 164.8 mm. Besides, the future PET is projected to increase for all seasons (Fig. 12b). Due to the relatively large amount of precipitation and the low rate of PET arising from the low temperature in winter, a relatively high winter streamflow is projected (Fig. 12e). For the Mission river basin, the average precipitation and PET are expected to rise for all seasons (Fig. 12c, d). In particular, there will be a considerable increase in the projected summer and fall precipitation of up to 35.2% and 23.3%, respectively, resulting in the relatively high summer and fall streamflow (Fig. 12f). Nevertheless, Fig. 12f shows a considerable decrease in streamflow during the fall season. This is because the

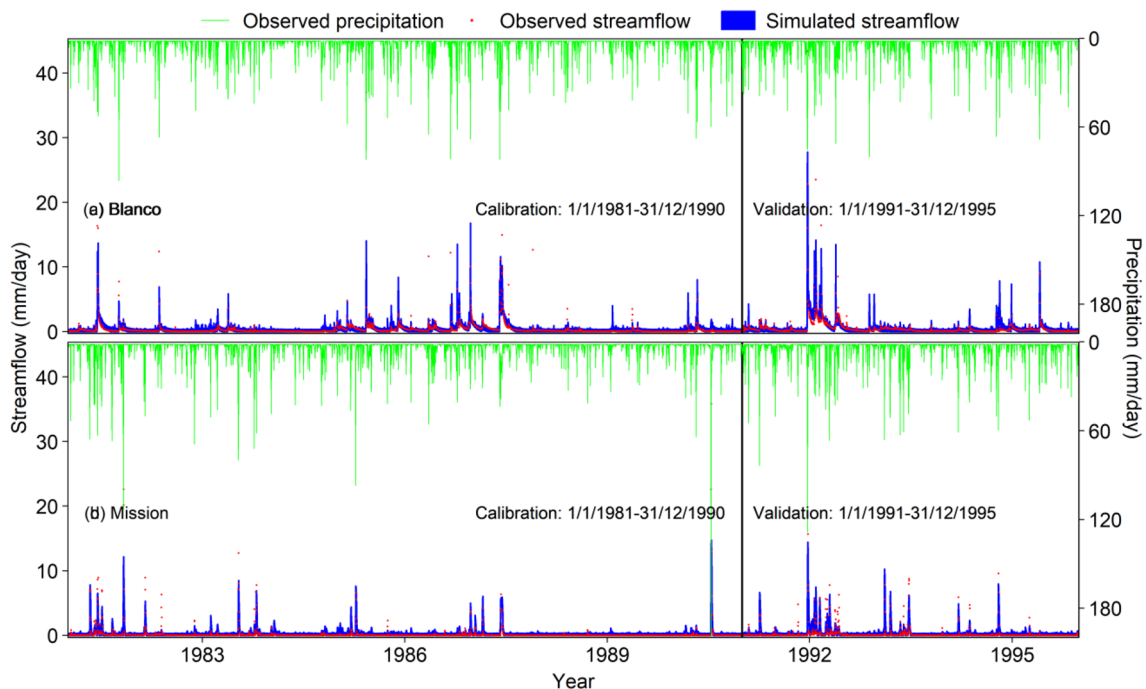
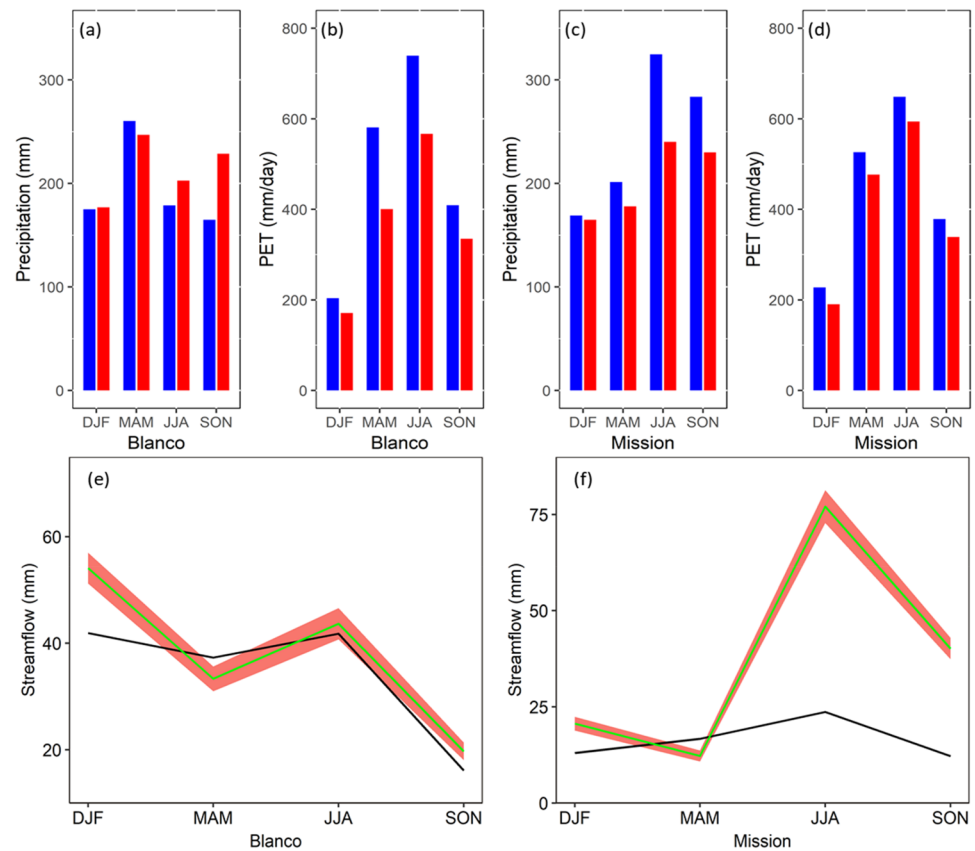


Fig. 11 Daily rainfall-runoff predictions over a period of 15 years (1981–1995). Blue areas represent the streamflow time series with the 95% uncertainty range. Red dots represent streamflow observations. The green line represents precipitation observations

Fig. 12 **a, c** Projected changes in seasonal mean precipitation during 2085–2099 compared to those during 1981–1995. Red and blue bars represent past and future seasonal precipitation, respectively. **b, d** Projected changes in seasonal mean PET during 2085–2099 compared to those during 1981–1995. Red and blue bars represent past and future seasonal PET, respectively. **e, f** Projected changes in seasonal streamflow during 2085–2099 compared to those during 1981–1995. Black and green lines represent the past seasonal streamflow and the future seasonal mean streamflow, respectively. The red shaded area represents the future seasonal streamflow with the 95% uncertainty range



summer streamflow can be largely used for irrigation as well as for municipal and industrial water supplies, resulting in a decline in surface water storage and the consequent decrease in streamflow for the fall season. Consequently, streamflow forecasts can help water managers to better use water resources in the season with abundant rainfall and to assess the potential risk of droughts during the dry season, as well as to make effective and timely decisions on sustainable development and disaster risk reduction goals.

3.4 Probabilistic projection of future changes in multivariate drought characteristics

To analyze the future changes in multivariate drought characteristics, the time series of the SHDI values can be estimated using copula functions based on the projected hydroclimatic variables. Figure 13 presents the comparison of the past and future time series of the SHDI values with uncertainty intervals across 3-, 9-, and 15-months timescales for the Blanco and the Mission river basins. The SHDI intervals are derived due to the uncertainties in model and copula parameters, and their upper and lower bounds represent the drought events under the best- and worst-case scenarios, respectively. It should be noted that more attention should be paid to the worst-case drought scenario that implies the

maximum risk of joint drought events, which facilitates the reduction of potential losses caused by drought hazards.

Although the temporal variations of the 3-, 9-, and 15-months future SHDI values are generally consistent with those in the historical period for the two river basins (Fig. 13), there is a large difference in drought characteristics including the frequency, the longest duration, and the average severity. The statistics of past and future multivariate drought characteristics are summarized under best- and worst-case scenarios, as shown in Table S8 of the supplementary material. Even though the frequency of the 3-, 9-, and 15-months future SHDI will decrease in comparison with the historical droughts, the longest duration and the average severity of droughts are expected to experience a significant increase for the Blanco river basin over the period of 2085–2099. For instance, the longest duration and the average severity of the long-term drought events are expected to increase to 94 months and -3.106 , respectively, under the worst-case scenario. By contrast, the longest duration and the average severity of the long-term historical drought events are only 32 months and -1.561 , respectively. This indicates that the future drought severity and duration are projected to greatly increase in the Blanco river basin under global warming.

The Mission river basin is located far away from urban areas, and thus there is a large difference in the projected

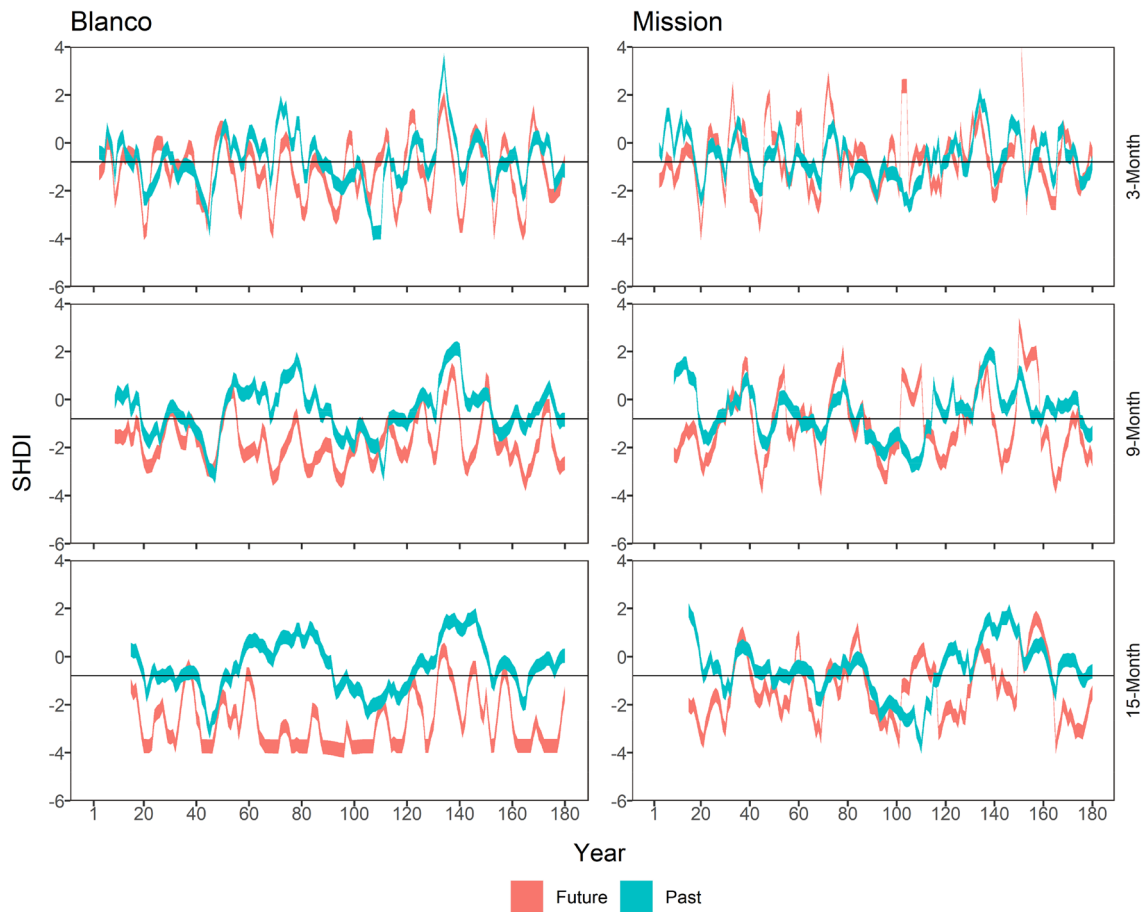


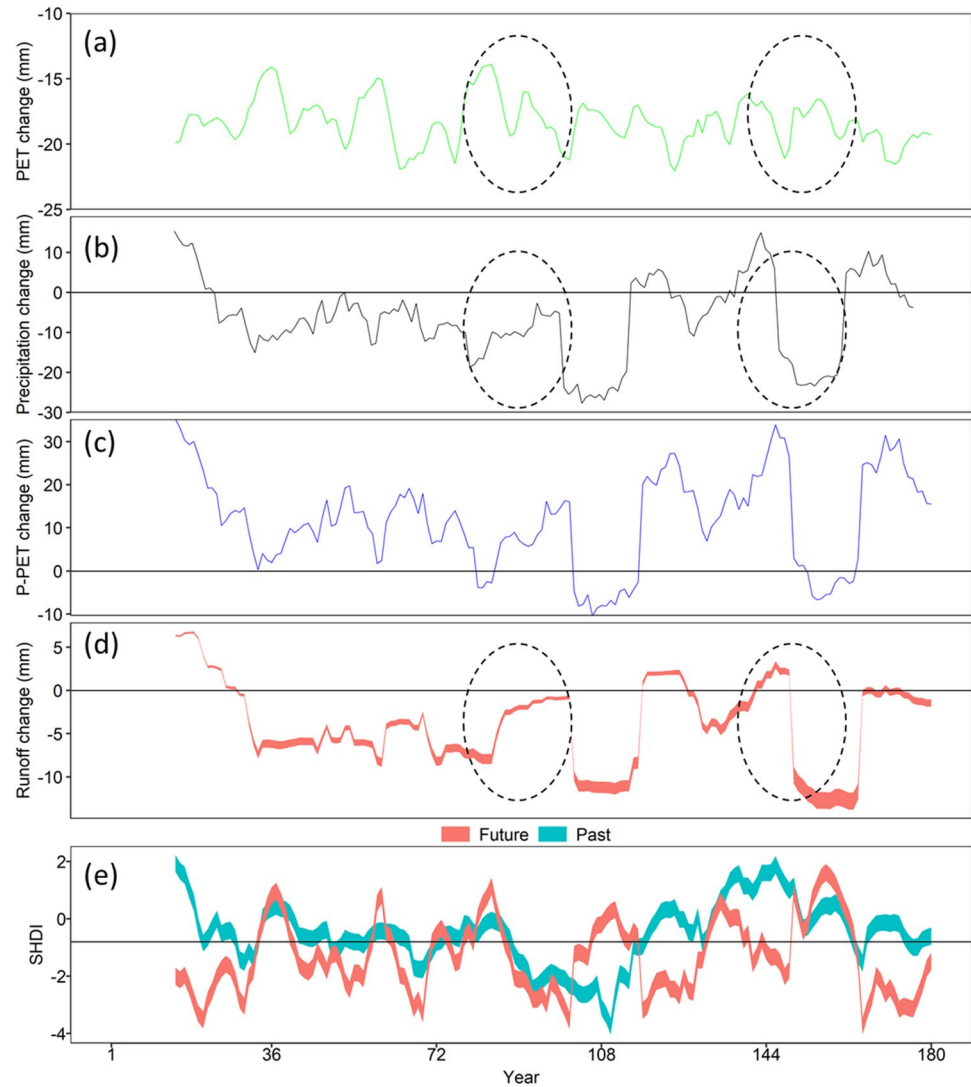
Fig. 13 Comparison of multivariate drought characteristics in past and future climates based on 3-, 9-, and 15-months SHDI

drought characteristics compared with those in the Blanco river basin due to the spatial heterogeneity of river basins such as soil conditions, land use types, and topography. In particular, the longest duration of droughts is projected to become shorter than the past. The longest duration of future drought events, across the timescales of 3, 9, and 15 months, is projected to last for 10, 22, and 20 months, respectively. In comparison, the longest duration of 3-, 9-, and 15-monthly historical droughts is 32, 28, and 31, respectively. In addition, the average severity of future droughts is expected to increase slightly. This implies that the Mission river basin will experience a slight increase in the severity of droughts over a shorter period of time. Our results indicate that droughts severity will become more severe even though there will be a decreasing number of drought episodes by the end of this century, especially for the long-term droughts. Moreover, the river basins with spatial heterogeneity may experience substantial difference in potential variations of drought characteristics.

Further investigations were also conducted to identify the dominant hydroclimatic variables influencing future

multivariate drought characteristics. Figure 14 shows the temporal variations in the 15-month PET, precipitation, P–PET, runoff, and SHDI for past and future periods in the Mission river basin. It can be seen that there is a high degree of similarity between precipitation and runoff changes (Fig. 14b, d). For example, the precipitation changes in dashed circles are projected to increase or decrease, and the runoff changes are then expected to increase or decrease accordingly. However, PET and runoff changes are completely opposite (Fig. 14a, d). PET is predicted to rise greatly for the future period 2085–2099. When PET increases, most of precipitation will be absorbed by dry soils, and then the soil water will evaporate rapidly as a result of the rising air temperature, resulting in a decline in runoff. Furthermore, the wet events are projected to decrease in a changing climate although future extreme precipitation events will increase in frequency and intensity, exacerbating the deficiency of runoff. Thus, droughts are projected to occur more severely and intensely by the end of this century.

Fig. 14 Temporal variations in the 15-months PET, precipitation, P-PET, runoff, and SHDI in the Mission river basin for past and future periods



3.5 Probabilistic projection of future changes in flood risks

Based on daily projected streamflow time series, the future flood events were sampled using the threshold estimates and the corresponding hydrographs introduced in Sect. 2.3. Figure 15 presents the T_{OR} and T_{AND} return periods of flood events in the Blanco and Mission river basins for the future period of 2085–2099. The Blanco and Mission river basins are expected to experience 32 and 21 flood events, respectively. Compared to the past (1981–1995), the flood peak and volume are expected to increase for both the Blanco and Mission river basins, which is largely due to the increase in the extreme precipitation over the two river basins. In addition, the frequency of flood events occurred in the Blanco river basin is projected to increase. By contrast, although the frequency of future flood events is projected to decrease over the Mission river basin, the flood peak and volume

are expected to increase. This reveals that there will be an increasing number of flood events with the larger volume as expected under global warming.

Figure 15 depicts the uncertainty intervals in the estimation of future flood return periods for the Blanco and Mission river basins. There is an apparent increase in future flood return periods for the Blanco river basin, with the mean T_{OR} and T_{AND} return periods of 2.4 and 23.8 years, respectively. In addition, the T_{AND} return period of flood events is projected to experience three 100-year floods over the Blanco river basin during 2085–2099. Similarly, the Mission river basin is also expected to experience an increase in the flood return period for both T_{OR} and T_{AND} cases, and the mean T_{OR} and T_{AND} return periods are 2.5 and 13.8 years, respectively. Moreover, the maximum T_{OR} and T_{AND} flood return periods are expected to reach 10 and 100 years, respectively, for the Mission river basin. These are much larger than those for the historical period. Overall, the intensity and discharge

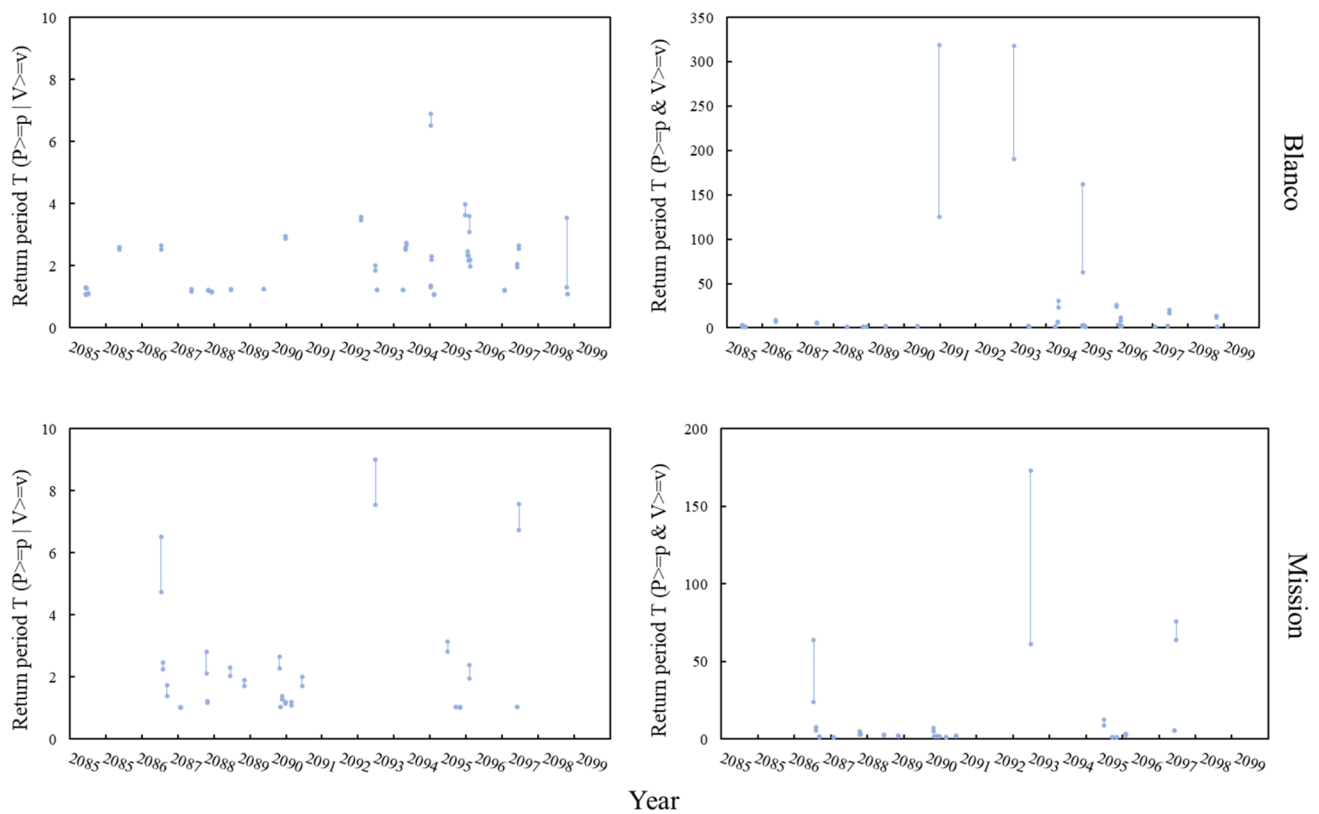


Fig. 15 Comparison of T_{OR} and T_{AND} flood return periods in the future for the Blanco and Mission river basins. The blue line represents the 95% uncertainty range of return periods

volume of flood events will increase for both the Blanco and Mission river basins by the end of this century. Furthermore, the Blanco and Mission river basins will face a higher risk of floods as both the T_{OR} and T_{AND} flood return periods becomes longer.

4 Summary and conclusions

In this study, we develop probabilistic projections of future changes in multidimensional drought and flood characteristics through the convection-permitting WRF modeling system. In addition, a copula-based SHDI approach is proposed to examine the joint effect of meteorological and hydrological droughts, and the joint effect of flood peak and volume is also examined to assess flood risks. Furthermore, the model and copula parameter uncertainties are addressed explicitly, leading to probabilistic projections of hydrological extremes for two major river basins of Texas.

Our findings reveal that the probabilistic assessment of hydrological extremes is able to reduce underestimation and bias arising from univariate analysis. Compared with SPEI and SRI, SHDI shows better skills in detecting extreme droughts that have widespread impacts on water security,

agricultural production, food security, and environmental sustainability. We argue that more attention should be paid in practice to the worst-case scenario of SHDI, which enables a conservative assessment of drought severity and provides meaningful insights into drought mitigation and preparedness. In addition, we find that the future droughts are expected to become more severe even though the frequency of the occurrence of droughts is projected to decrease in a changing climate, especially for the long-term drought episodes. On the other hand, the frequency and volume of flood events are projected to increase for the Blanco river basin. By contrast, the flood intensity and volume will increase even though there will be a decreasing number of flood events for the Mission river basin. Furthermore, there is an apparent increase in the flood return period for both the Blanco and Mission river basins by the end of the twenty-first century, which indicates that the two basins will suffer from higher flood risks under global warming. Overall, the future dry days and extreme precipitation events are projected to occur more frequently and intensely, thereby increasing the risk of droughts and flash floods over South Texas.

It should be noted that parameter uncertainties were addressed in this study. Nevertheless, the other sources of

uncertainty, including uncertainties in forcing/input data and model structure, should also be tackled to further improve the reliability of drought and flood assessments. In addition, the future climate change projection was carried out under the business-as-usual scenario RCP8.5 with continuously increasing greenhouse gas emissions over time, the projected severity of droughts and floods would vary under other scenarios in which CO₂ emissions are controlled.

Acknowledgements This research was supported by the National Natural Science Foundation of China (Grant No. 51809223) and the Hong Kong Polytechnic University Start-up Grant (Grant No. 1-ZE8S). The daily rainfall and runoff observations for Blanco and Mission river basins were collected from the U.S. MOPEX dataset. The PRISM dataset was produced by the PRISM Climate Group at Oregon State University and the CFSR product was provided by the NCEP. We would like to express our sincere gratitude to the editor and anonymous reviewers for their constructive comments and suggestions.

References

- Abera W, Formetta G, Brocca L, Rigon R (2017) Modeling the water budget of the Upper Blue Nile basin using the JGrass-NewAge model system and satellite data. *Hydrol Earth Syst Sci* 21:3145–3165. <https://doi.org/10.5194/hess-21-3145-2017>
- Adamson PT, Metcalfe AV, Parmentier B (1999) Bivariate extreme value distributions: an application of the Gibbs sampler to the analysis of floods. *Water Resour Res* 35(9):2825–2832
- Allen RG, Pereira LS, Raes D, Smith M (1998) Crop evapotranspiration—Guidelines for computing crop water requirements, Irrigation and Drainage Paper No. 56. Food and Agriculture Organization of the United Nations, Rome
- Carvalho KS, Wang S (2019) Characterizing the Indian Ocean sea level changes and potential coastal flooding impacts under global warming. *J Hydrol* 569:373–386. <https://doi.org/10.1016/j.jhydrol.2018.11.072>
- Chebana F, Ouarda TBMJ, Bruneau P (2009) Multivariate homogeneity testing in a northern case study in the province of Quebec. *Can Hydrol Process* 23(12):1690–1700
- Chen H, Wang S, Wang Y (2020) Exploring abrupt alternations between wet and dry conditions on the basis of historical observations and convection-permitting climate model simulations. *J Geophys Res Atmos*. <https://doi.org/10.1029/2019JD031982>
- Chen X, Li F, Li J et al (2019) Three-dimensional identification of hydrological drought and multivariate drought risk probability assessment in the Luanhe River basin, China. *Theor Appl Climatol*. <https://doi.org/10.1007/s00704-019-02780-5>
- Cheraghalizadeh M, Ghameshlou AN, Bazrafshan J et al (2018) A copula-based joint meteorological-hydrological drought index in a humid region (Kasilian basin, North Iran). *Arab J Geosci* 11:300. <https://doi.org/10.1007/s12517-018-3671-7>
- DeChant CM, Moradkhani H (2015) On the assessment of reliability in probabilistic hydrometeorological event forecasting. *Water Resour Res* 51:3867–3883. <https://doi.org/10.1002/2014WR016617>
- De Michele C, Salvadori G, Passoni G, Vezzoli R (2007) A multivariate model of sea storms using copulas. *Coast Eng* 54:734–751. <https://doi.org/10.1016/j.coastaleng.2007.05.007>
- De Michele C, Salvadori G, Canossi M, Petaccia A, Rosso R (2005) Bivariate statistical approach to check adequacy of dam spillway. *J Hydrol Eng* 10:50–57. [https://doi.org/10.1061/\(ASCE\)1084-0699\(2005\)10:1\(50\)](https://doi.org/10.1061/(ASCE)1084-0699(2005)10:1(50))
- Favre A, El Adlouni S, Perreault L, Thiémonge N, Bobeé B (2004) Multivariate hydrological frequency analysis using copulas. *Water Resour Res* 40:W01101. <https://doi.org/10.1029/2003WR002456>
- Flint LE, Flint AL, Mendoza J et al (2018) Characterizing drought in California: new drought indices and scenario-testing in support of resource management. *Ecol Process* 7:1. <https://doi.org/10.1186/s13717-017-0112-6>
- Genest C, Favre A (2007) Everything you always wanted to know about copula modeling but were afraid to ask. *J Hydrol Eng* 12:347–368. [https://doi.org/10.1061/\(ASCE\)1084-0699\(2007\)12:4\(347\)](https://doi.org/10.1061/(ASCE)1084-0699(2007)12:4(347))
- Goel NK, Seth SM, Chandra S (1998) Multivariate modeling of flood flows. *J Hydraul Eng* 124(2):146–155
- Hao C, Zhang J, Yao F (2017) Multivariate drought frequency estimation using copula method in southwest China. *Theor Appl Climatol* 127:977–991. <https://doi.org/10.1007/s00704-015-1678-5>
- Hao Z, AghaKouchak A (2013) Multivariate Standardized Drought Index: a parametric multi-index model. *Adv Water Resour* 57:12–18. <https://doi.org/10.1016/j.advwatres.2013.03.009>
- Hao Z, Singh VP (2015) Drought characterization from a multivariate perspective: a review. *J Hydrol* 527:668–678. <https://doi.org/10.1016/j.jhydrol.2015.05.031>
- Hong SY, Pan HL (1996) Nonlocal boundary layer vertical diffusion in a medium-range forecast model. *Mon Weather Rev* 124:2322–2339. [https://doi.org/10.1175/1520-0493\(1996\)124<2322:NBLVDI>2.0.CO;2](https://doi.org/10.1175/1520-0493(1996)124<2322:NBLVDI>2.0.CO;2)
- Iacono MJ, Delamere JS, Mlawer EJ, Shephard MW, Clough SA, Collins WD (2008) Radiative forcing by long-lived greenhouse gases: calculations with the AER radiative transfer models. *J Geophys Res Atmos* 113:D13103. <https://doi.org/10.1029/2008JD009944>
- Jimenez PA, Dudhia J, Gonzalez-Rouco JF, Navarro J, Montavez JP, Garcia-Bustamante E (2012) A revised scheme for the WRF surface layer formulation. *Mon Weather Rev* 140:898–918. <https://doi.org/10.1175/MWR-D-11-00056.1>
- Kao SC, Govindaraju RS (2008) Trivariate statistical analysis of extreme rainfall events via the Plackett family of copulas. *Water Resour Res* 44:W02415. <https://doi.org/10.1029/2007WR006261>
- Kao SC, Govindaraju RS (2010) A copula-based joint deficit index for droughts. *J Hydrol* 380:121–134. <https://doi.org/10.1016/j.jhydrol.2009.10.029>
- Karri S, Dash SK, Panda SK et al (2018) Relative role of sea surface temperature and snow on Indian summer monsoon seasonal simulation using a GCM. *Arab J Geosci* 11:210. <https://doi.org/10.1007/s12517-018-3559-6>
- Kavianpour M, Seyedabadi M, Moazami S (2018) Spatial and temporal analysis of drought based on a combined index using copula. *Environ Earth Sci* 77:769. <https://doi.org/10.1007/s12665-018-7942-0>
- Kay AL, Rudd AC, Davies HN et al (2015) Use of very high resolution climate model data for hydrological modelling: baseline performance and future flood changes. *Climatic Change* 133:193. <https://doi.org/10.1007/s10584-015-1455-6>
- Kwon H, Lall U (2016) A copula-based nonstationary frequency analysis for the 2012–2015 drought in California. *Water Resour Res* 52:5662–5675. <https://doi.org/10.1002/2016WR018959>
- Lange S, Rockel B, Volkholz J et al (2015) Regional climate model sensitivities to parametrizations of convection and non-precipitating subgrid-scale clouds over South America. *Clim Dyn* 44:2839. <https://doi.org/10.1007/s00382-014-2199-0>
- Li K, Huang G, Wang S (2019) Market-based stochastic optimization of water resources systems for improving drought resilience and economic efficiency in arid regions. *J Clean Prod* 233:522–537. <https://doi.org/10.1016/j.jclepro.2019.05.379>
- Liu C et al (2017) Continental-scale convection-permitting modeling of the current and future climate of North America. *Clim Dyn* 49:71–95. <https://doi.org/10.1007/s00382-016-3327-9>
- Liu C, Ikeda K, Thompson G, Rasmussen R, Dudhia J (2011) High-resolution simulations of wintertime precipitation in the Colorado

- Headwaters region: sensitivity to physics parameterizations. *Mon Weather Rev* 139:3533–3553. <https://doi.org/10.1175/MWR-D11-00009.1>
- Lloyd-Hughes B, Saunders MA (2002) A drought climatology for Europe. *Int J Climat* 22:571–1592. <https://doi.org/10.1002/joc.846>
- Miah MG, Abdullah HM, Jeong C (2017) Exploring standardized precipitation evapotranspiration index for drought assessment in Bangladesh. *Environ Monit Assess* 189:547. <https://doi.org/10.1007/s10661-017-6235-5>
- Mishra AK, Singh VP (2010) A review of drought concepts. *J Hydrol* 391:202–216. <https://doi.org/10.1016/j.jhydrol.2010.07.012>
- Moore RJ (1985) The probability-distributed principle and runoff production at point and basin scales. *Hydrol Sci J* 30:273–297. <https://doi.org/10.1080/02626668509490989>
- Nalbantis I, Tsakiris G (2009) Assessment of hydrological drought revisited. *Water Resour Manage* 23:881–897. <https://doi.org/10.1007/s11269-008-9305-1>
- Niu GY et al (2011) The community Noah land surface model with multiparameterization options (Noah-MP): 1. Model description and evaluation with local-scale measurements. *J Geophys Res Atmos* 116:D12109. <https://doi.org/10.1029/2010JD015139>
- Prein AF et al (2015) A review on regional convection-permitting climate modeling: demonstrations, prospect, and challenges. *Rev Geophys* 53:323–361. <https://doi.org/10.1002/2012RG000457>
- Parry M, Canziani O, Palutikof J et al (2007) *Climate change 2007: impacts, adaptation and vulnerability; Contribution of Working Group II to the fourth assessment report of the Intergovernmental Panel on Climate Change*. Cambridge University Press, Cambridge
- Razavi S, Gupta HV (2016) A new framework for comprehensive, robust, and efficient global sensitivity analysis: 2. Application. *Water Resour Res* 52:440–455. <https://doi.org/10.1002/2015WR017559>
- Raziei T, Saghaian B, Paulo AA et al (2009) Spatial patterns and temporal variability of drought in western Iran. *Water Resour Manage* 23:439. <https://doi.org/10.1007/s11269-008-9282-4>
- Roy T, Gupta HV, Serrat-Capdevila A, Valdes JB (2017) Using satellite-based evapotranspiration estimates to improve the structure of a simple conceptual rainfall–runoff model. *Hydrol Earth Syst Sci* 21:879–896. <https://doi.org/10.5194/hess-21-879-2017>
- Sadegh M, Ragno E, AghaKouchak A (2017) Multivariate Copula Analysis Toolbox (MvCAT): Describing dependence and underlying uncertainty using a Bayesian framework. *Water Resour Res* 53:5166–5183. <https://doi.org/10.1002/2016WR020242>
- Salvadori G, De Michele C (2015) Multivariate real-time assessment of droughts via copula-based multi-site Hazard Trajectories and Fans. *J Hydrol* 526:101–115. <https://doi.org/10.1016/j.jhydrol.2014.11.056>
- Sexton D, Rowell D, Folland C et al (2001) Detection of anthropogenic climate change using an atmospheric GCM. *Clim Dyn* 17:669. <https://doi.org/10.1007/s003820000141>
- Shukla S, Wood AW (2008) Use of a standardized runoff index for characterizing hydrologic drought. *Geophys Res Lett* 35:226–236. <https://doi.org/10.1029/2007GL032487>
- Song X, Song S, Sun W, Mu X, Wang S, Li J, Li Y (2015) Recent changes in extreme precipitation and drought over the Songhua River Basin, China, during 1960–2013. *Atmos Res* 157:137–152. <https://doi.org/10.1016/j.atmosres.2015.01.022>
- Tabari H, Nikbakht J, Hosseinzadeh Talaei P (2013) Hydrological drought assessment in northwestern Iran based on streamflow drought index (SDI). *Water Resour Manage* 27:137. <https://doi.org/10.1007/s11269-012-0173-3>
- Thompson G, Field PR, Rasmussen RM, Hall WD (2008) Explicit forecasts of winter precipitation using an improved bulk microphysics scheme. Part II: Implementation of a new snow parameterization. *Mon Wea Rev* 136:5095–5115. <https://doi.org/10.1175/2008MWR2387.1>
- Vicente-Serrano SM, López-Moreno JI, Beguería S, Lorenzo-Lacruz J, Azorin-Molina C, Morán-Tejada E (2011) Accurate computation of a streamflow drought index. *J Hydrol Eng* 17:318–332. [https://doi.org/10.1061/\(ASCE\)HE.1943-5584.000043](https://doi.org/10.1061/(ASCE)HE.1943-5584.000043)
- Wagner S, Berg P, Schädler G et al (2013) High resolution regional climate model simulations for Germany: Part II—projected climate changes. *Clim Dyn* 40:415. <https://doi.org/10.1007/s00382-012-1510-1>
- Wang S, Ancell BC, Huang GH, Baetz BW (2018) Improving robustness of hydrologic ensemble predictions through probabilistic pre- and post-processing in sequential data assimilation. *Water Resour Res* 54:2129–2151. <https://doi.org/10.1002/2018WR022546>
- Wang S, Wang Y (2019) Improving probabilistic hydroclimatic projections through high-resolution convection-permitting climate modeling and Markov chain Monte Carlo simulations. *Clim Dyn* 53:1613–1636. <https://doi.org/10.1007/s00382-019-04702-7>
- Wang S, Zhu J (2020) Amplified or exaggerated changes in perceived temperature extremes under global warming. *Clim Dyn* 54:117–127. <https://doi.org/10.1007/s00382-016-3327-9>
- Waseem M, Ajmal M, Lee JH et al (2016) Multivariate drought assessment considering the antecedent drought conditions. *Water Resour Manage* 30:4221. <https://doi.org/10.1007/s11269-016-1416-5>
- Xiao M, Zhang Q, Singh VP, Chen X (2016) Probabilistic forecasting of seasonal drought behaviors in the Huai River basin, China. *Theor Appl Climatol* 128:667–677. <https://doi.org/10.1007/s00704-016-1733-x>
- Yang ZL et al (2011) The community Noah land surface model with multiparameterization options (Noah-MP): 2. Evaluation over global river basins. *J Geophys Res Atmos* 116:D12111. <https://doi.org/10.1029/2010JD015140>
- Yue S (2000) The bivariate lognormal distribution to model a multivariate flood episode. *Hydrol Process* 14:2575–2588
- Yue S (2001) A bivariate gamma distribution for use in multivariate flood frequency analysis. *Hydrol Process* 15:1033–1045
- Zhang B, Wang S, Wang Y (2019) Copula-based convection-permitting projections of future changes in multivariate drought characteristics. *J Geophys Res Atmos*. <https://doi.org/10.1029/2019JD030686>
- Zhang D, Yan D, Lu F, Wang Y, Feng J (2015) Copula-based risk assessment of drought in Yunnan Province, China. *Nat Hazards* 75:2199–2220. <https://doi.org/10.1007/s11069-014-1419-6>
- Zhu J, Wang S, Huang G (2019) Assessing climate change impacts on human-perceived temperature extremes and underlying uncertainties. *J Geophys Res Atmos* 124:3800–3821. <https://doi.org/10.1029/2018JD029444>
- Zuo D, Cai S, Xu Z, Li F, Sun W, Yang X, Kan G, Liu P (2016) Spatial-temporal patterns of drought at various time scales in Shandong Province of eastern China. *Theor Appl Climatol* 131:271–284. <https://doi.org/10.1007/s00704-016-1969-5>